

# DWI of the Spinal Cord with Reduced FOV Single-Shot EPI

Emine Ulku Saritas,<sup>1\*</sup> Charles H. Cunningham,<sup>2</sup> Jin Hyung Lee,<sup>1</sup> Eric T. Han,<sup>3</sup>  
and Dwight G. Nishimura<sup>1</sup>

**Single-shot echo-planar imaging (ss-EPI) has not been used widely for diffusion-weighted imaging (DWI) of the spinal cord, because of the magnetic field inhomogeneities around the spine, the small cross-sectional size of the spinal cord, and the increased motion in that area due to breathing, swallowing, and cerebrospinal fluid (CSF) pulsation. These result in artifacts with the usually long readout duration of the ss-EPI method. Reduced field-of-view (FOV) methods decrease the required readout duration for ss-EPI, thereby enabling its practical application to imaging of the spine. In this work, a reduced FOV single-shot diffusion-weighted echo-planar imaging (ss-DWEPI) method is proposed, in which a 2D spatially selective echo-planar RF excitation pulse and a 180° refocusing pulse reduce the FOV in the phase-encode (PE) direction, while suppressing the signal from fat simultaneously. With this method, multi slice images with higher in-plane resolutions ( $0.94 \times 0.94 \text{ mm}^2$  for sagittal and  $0.62 \times 0.62 \text{ mm}^2$  for axial images) are achieved at 1.5 T, without the need for a longer readout. Magn Reson Med 60:468–473, 2008. © 2008 Wiley-Liss, Inc.**

**Key words:** diffusion weighted imaging; spinal cord; reduced FOV; EPI

## INTRODUCTION

Diffusion imaging of the spinal cord has recently become a subject of interest, since it has potential to help understand and diagnose many disorders resulting from damage to the long fiber tracts. However, in vivo DWI of the spinal cord is challenging because of the magnetic field inhomogeneities around the spine (1,2) that result in off-resonance related artifacts and limit the readout duration. Partial volume effects due to the surrounding CSF and lipid cause further artifacts; and the images are distorted due to susceptibility variations. Furthermore, the cross-sectional size of the spinal cord is relatively small (around 1 cm in diameter at its widest point), requiring smaller voxels for reasonable spatial resolution. An additional difficulty is the bulk physiologic motion around the spinal cord due to CSF pulsation, oscillatory spinal cord motion synchronized to cardiac cycle (3), breathing, swallowing, etc., which results in a zeroth-order phase error and a shift from the center of  $k$ -space if the motion occurs during the diffusion sensitiz-

ing magnetic field gradients ( $G_{\text{Diff}}$ ) (4). These phase errors differ for each repetition time (TR), manifesting themselves as ghosting artifacts in the multi shot diffusion-weighted (DW) image, and an overestimation of the apparent diffusion coefficient (ADC). All of these factors add up, yielding very low-signal, low-resolution DW images for the spinal cord with artifacts.

The most frequently used technique for DWI, especially for the brain, remains ss-EPI (5). Because the ss-EPI sequence acquires the whole of  $k$ -space after a single excitation pulse, the magnitude images do not suffer from the ghosting artifacts arising from motion-induced phase errors. The drawbacks of the ss-EPI method are the long readout that experiences  $T_2^*$  decay, causing severe blurring of the images along the PE direction, and the long interval between subsequent  $k$ -space profiles that result in significant phase errors due to off-resonance (e.g., from chemical shift,  $B_0$ -inhomogeneities, susceptibility gradients, eddy currents). Furthermore, the water-fat chemical shift artifact in ss-EPI, which can be quite substantial, needs to be avoided by using either fat suppression or spectrally selective excitation. In view of these facts, and considering the magnetic field inhomogeneities around the spine, it is particularly difficult to produce ss-EPI images of the spinal cord with sufficient quality.

Recently, spinal cord imaging has been shown to benefit from reduced FOV applications because of its long and narrow anatomy and small cross-sectional size (6–8). In general, reduced FOV methods decrease the readout duration needed for imaging, thereby reducing off-resonance induced artifacts and enabling the usage of the ss-EPI technique for the spine. This work describes reduced FOV ss-DWEPI of the spinal cord, where the excited FOV in the PE direction is reduced by using a 2D spatially selective echo-planar RF excitation pulse, followed by a 180° refocusing RF pulse. The required number of  $k$ -space lines in the PE direction is decreased by reducing the FOV, enabling higher resolution imaging for a fixed scan time. Furthermore, the combination of the 2D RF pulse and the 180° refocusing RF pulse allows multi slice imaging, while simultaneously suppressing the signal from fat. With this method, contiguous slices can be obtained without any slice gap as needed in ZOOM-EPI (6). Instead of using additional outer volume suppression pulses as in (7), this method actively excites only the parts of the volume that will be used for imaging. Also, unlike using multiple 1D excitation pulses (8), here the resulting signal-to-noise ratio (SNR) does not depend on the number of slices.

## THEORY

The pulse sequence used in this work is a standard DW spin-echo ss-EPI sequence, with the excitation pulse replaced with a 90° 2D spatially selective echo-planar RF pulse that reduces the FOV in the PE direction. The details

<sup>1</sup>Magnetic Resonance Systems Research Laboratory, Department of Electrical Engineering, Stanford University, Stanford, California

<sup>2</sup>Sunnybrook Health Sciences Centre, University of Toronto, Toronto, Canada

<sup>3</sup>GE Healthcare Global Applied Science Laboratory, Menlo Park, California

Grant sponsors: Lucent Technologies Stanford Graduate Fellowship, GE Healthcare.

\*Correspondence to: Emine Ulku Saritas, Packard Electrical Engineering, Room 210, 350 Serra Mall, Stanford, CA 94305-9510.  
E-mail: saritas@stanford.edu

Received 12 October 2007; revised 6 February 2008; accepted 3 March 2008.

DOI 10.1002/mrm.21640

Published online in Wiley InterScience (www.interscience.wiley.com).

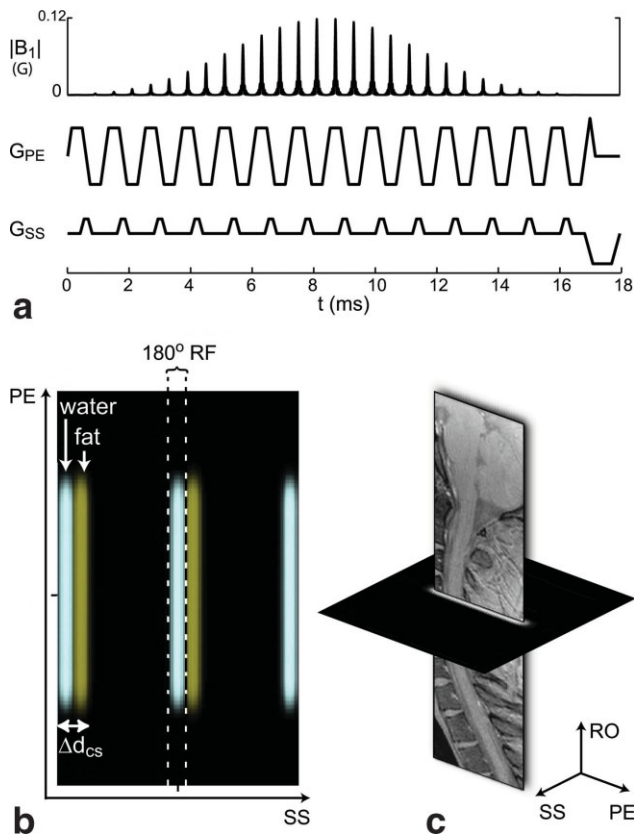


FIG. 1. (a) 2D echo-planar RF pulse and (b) simulation of the excitation profile showing how the 2D RF pulse and refocusing  $180^\circ$  RF pulse pair select water only in the main lobe (color coded for illustration purposes). Note that water and fat profiles are shifted by  $\Delta d_{cs}$  in the SS-direction. (c) The resulting water slice and slab profile shown in 3D, along with the reduced FOV image.

of the 2D RF pulse and its multi slice imaging compatibility are explained in the following sections.

## 2D Echo-Planar RF Pulse

2D echo-planar RF pulses provide independent control of slice thickness in two orthogonal directions by combining two RF pulses that can be designed separately. Using a rectilinear path in the excitation  $k$ -space in the shape of an EPI trajectory, the “slow” (blipped) and the “fast” axes gradients and RF pulses are designed to achieve the desired excitation profiles in each spatial direction (9). The 2D echo-planar RF pulse used in this work (Fig. 1a) generates a  $90^\circ$  flip angle over a  $4 \text{ mm} \times 4.5 \text{ cm}$  slab. Here, the two orthogonal directions are the slice-select (SS) direction and the slab-select direction, where the latter is the PE direction during imaging. As a result of this excitation scheme, the 2D RF pulse reduces the excited FOV in the PE direction to 4.5 cm. The duration of the 2D RF pulse is 16.8 ms, with the number of blips  $N_{\text{blip}} = 14$  in the SS direction. Time-bandwidth (TBW) products in the PE and SS directions are  $TBW_{\text{PE}} = 12$  and  $TBW_{\text{SS}} = 3$ , correspondingly.

The simulated excitation profiles for fat and water (assuming a chemical shift of 220 Hz at 1.5 T) are shown in Fig. 1b. Note that the excitation profile in the SS direction is periodic, because the blipped gradients in that direction

fill the RF excitation  $k$ -space discretely. Also note that the excitation profiles for fat and water are displaced in volume along the blipped (SS) direction. This spatial displacement ( $\Delta d_{cs}$ ), caused by the echo-planar path of the 2D RF excitation pulse and the off-resonance between fat and water, is given by:

$$\Delta d_{cs} = \frac{N_{\text{blip}} f_{cs} T_{\text{fast}}}{K_{\text{blip}}}, \quad [1]$$

where  $N_{\text{blip}}$  is the number of blips,  $f_{cs}$  is the chemical shift in Hertz,  $T_{\text{fast}}$  is the duration of a fast gradient lobe, and  $K_{\text{blip}}$  is the extent of  $k$ -space traversed in the blipped direction. Further details of 2D echo-planar RF pulse design can be found in (9).

In our 2D RF pulse, the displacement  $\Delta d_{cs}$  between fat and water is designed to be such that the excited fat profile is completely outside the excited water profile. All of the pulse design parameters (e.g.,  $TBW_{\text{PE}}$ ,  $TBW_{\text{SS}}$ , the pulse duration, and  $N_{\text{blip}}$ ) are chosen to both achieve the desired excitation profiles in PE and SS directions, while ensuring that the fat and water profiles do not overlap. Note that from Eq. [1], more blips (i.e., longer 2D RF pulses) are needed to make the fat profile shift further away from the water profile. More blips are also required for achieving a sharper slice profile and further separating the excitation sidelobes from the main lobe of the excitation. Furthermore, there is a trade-off between the peak  $B_1$  value versus the number of blips, which also has to be taken into account while designing the pulse. Reducing the number of blips while keeping the profile the same requires higher peak  $B_1$  values. In our design, the peak  $B_1$  value was kept at 0.12 Gauss, and the other design parameters were calculated accordingly.

After 2D RF excitation, we use a regular  $180^\circ$  refocusing RF pulse selective in the SS direction, with crusher gradients before and after the pulse. Note that by using the 2D RF pulse and the  $180^\circ$  refocusing RF pulse together, we suppress any signal from the outside lobes of the periodic 2D excitation, as well as the signal from fat (Fig. 1b). This fat suppression is especially important in EPI, where the fat component is dramatically shifted in the PE direction with respect to the water component, which can lead to undesired image artifacts if the signal from fat is not suppressed.

## Multi Slice Imaging

FOV restriction methods that use the intersection of two separate 1D RF pulses do not allow multi slice imaging. For example, a slab-selective excitation pulse in the PE direction followed by a slice-selective refocusing  $180^\circ$  pulse in the SS direction is not compatible with multi slice imaging, because the slab-selective excitation pulse excites the adjacent slices as well.

In contrast, the adjacent slices are not excited by the 2D echo-planar RF pulse, therefore, contiguous multi slice imaging is applicable. One important point to note is that, there is an upper limit for the number of slices that can be imaged simultaneously, which is determined by the number of slices that can fit between the two periodic lobes of the excitation profile. The maximum number of slices is:

$$\begin{aligned} \max(N_{\text{slices}}) &= \frac{\Delta d_{\text{replicate}}}{\Delta d_{\text{SS}}} \\ &= \frac{N_{\text{blip}}}{TBW_{\text{SS}}} \end{aligned} \quad [2]$$

where  $N_{\text{slices}}$  is the number of slices,  $\Delta d_{\text{replicate}}$  is the distance between the periodic lobes in the SS direction and  $\Delta d_{\text{SS}}$  is the slice thickness. In this work, three slices were used for sagittal imaging, which is enough to cover the whole spine for a slice thickness of 4 mm, since the spinal cord is around 1 cm in diameter. According to Eq. [2], to increase the maximum number of slices for a fixed slice profile, more blips are needed.

The whole pulse sequence (including the 90° 2D RF pulse, the 180° refocusing RF pulse, DW gradients, and the ss-EPI readout) takes less than 120 ms per slice, conveniently allowing multi slice imaging in a single cardiac cycle.

## METHODS

Phantom experiments and in vivo scans of healthy subjects were acquired using a 1.5 T GE Excite scanner, with 40 mT/m maximum gradient strength and 150 mT/(m ms) maximum slew rate.

### Phantom Experiments

A phantom filled with manganese chloride doped water and canola oil was imaged with a quadrature head coil to demonstrate the results of reducing the FOV and suppressing the signal from fat via the 2D selective RF pulse and 180° refocusing pulse pair. The phantom was first scanned with a conventional spin-echo pulse sequence. Other scan parameters were TE = 30 ms, TR = 500 ms, FOV = 12 × 12 cm<sup>2</sup>, 0.47 × 0.47 mm<sup>2</sup> in-plane resolution ( $k$ -space matrix = 256 × 256), slice thickness = 5 mm. The phantom was then scanned using the previously described 2D echo-planar RF pulse as the excitation pulse. To achieve a direct comparison, all the imaging parameters (other than the excitation pulse) were kept the same for both cases.

### In Vivo Imaging

In vivo sagittal images of the cervical spinal cord of a healthy subject were acquired using an 8-channel phased-array neurovascular coil. The reduced FOV imaging consisted of three adjacent slices with 0.5-mm slice spacing, 4-mm slice thickness, 18 × 4.5 cm<sup>2</sup> FOV, 0.94 × 0.94 mm<sup>2</sup> in-plane resolution (192 × 48 imaging matrix). A partial  $k$ -space percentage of 62.5% in the PE direction corresponding to an echo train length (ETL) of 30 lines was used. The total readout time was 52.5 ms with TE = 62.5 ms and ±62.5 kHz sampling bandwidth. For comparison, a full-FOV single slice ss-EPI sequence with the same number of data points and a similar readout time of 59 ms was used, for which the FOV in the PE direction was chosen such that no aliasing artifact occurs in the region of interest. The imaging parameters for this regular ss-EPI case were TE = 64.7 ms, 18 × 18 cm<sup>2</sup> FOV, 1.88 × 1.88 mm<sup>2</sup> in-plane resolution (96 × 96 imaging matrix), with a partial  $k$ -space percentage of 62.5%, corresponding to an ETL of 60 lines.

Stejskal-Tanner spin-echo diffusion-weighting gradients (10) were applied in the superior-inferior (SI), anterior-posterior (AP), and left-right (LR) directions, with a  $b$ -value of 500 s/mm<sup>2</sup>. Note that the optimum  $b$ -value that maximizes the SNR of the ADC map (11) is lower for the spinal cord than for the brain, with typical values of around 600 s/mm<sup>2</sup> used in the literature (1). This is because of the high ADC values measured in the white matter of the spinal cord in the SI-direction [an average of 1863 × 10<sup>-6</sup> mm<sup>2</sup>/s in healthy subjects (1)], which result in higher signal attenuation for a fixed  $b$ -value, when compared to brain DWI studies. Here, we have chosen  $b = 500$  s/mm<sup>2</sup> due to the SNR considerations further imposed by the high resolutions aimed in this work. Using a higher  $b$ -value is possible, with the trade-off being the quality of both the DW images and the ADC maps for a fixed scan time.

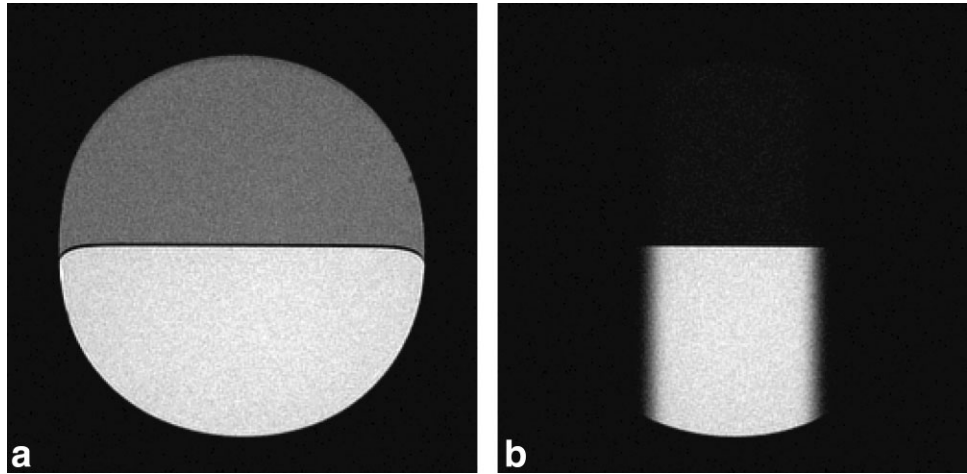
To avoid pulsatile cord and CSF motion, all imaging sequences were cardiac gated with trigger signal from a finger plethysmograph. To obtain sufficient  $T_1$  recovery, sequences were triggered every four cardiac cycles, during which three adjacent slices with a slice spacing of 0.5 mm were acquired simultaneously. After the systole peak is detected, a delay of 400 ms was employed to ensure minimum bulk motion during the diffusion sensitizing gradients (12). Depending on the heart rate, the total scan time for acquiring the non-DW image (DW<sub>0</sub>) and the DW images in all three directions (DW<sub>SI</sub>, DW<sub>AP</sub>, and DW<sub>LR</sub>) varied from 10 to 12 min. During this scan time, a total of 20 single-shot DW<sub>0</sub>, 60 DW<sub>SI</sub>, 40 DW<sub>AP</sub>, and 40 DW<sub>LR</sub> images were acquired.

To demonstrate the feasibility of high-resolution axial images of the cervical spinal cord with this scheme, we have also acquired images of the cervical spinal cord in the axial plane with 0.62 × 0.62 mm<sup>2</sup> in-plane resolution. These axial scans were conducted using an 8-channel head coil. As mentioned earlier, there is a limit on the maximum number of slices that can be imaged simultaneously. For 5-mm slice thickness and 0.5 mm slice spacing, four slices can be imaged simultaneously during a single TR. Other imaging parameters were  $b = 500$  s/mm<sup>2</sup>, TE = 67.7 ms, TR = 4 cardiac cycles, FOV = 8 × 3 cm<sup>2</sup>, 128 × 48 imaging matrix, 62.5% partial  $k$ -space coverage, ±31.25 kHz sampling bandwidth.

### Image Reconstruction

At the beginning of each scan, a reference scan was acquired with the PE gradients of EPI turned off (13). This reference data was used to correct for the ghosting artifacts arising from gradient delay, which results in a shift in  $k$ -space between even and odd-numbered echo lines. Refocusing reconstruction (14) was utilized to correct for shot-to-shot phase variations that result from motion during diffusion-sensitizing magnetic field gradients. The central 12.5% of  $k$ -space data from each single-shot DW image was used as the “navigator data” during calculations. This corresponds to navigator matrix sizes of 24 × 6 for the sagittal reduced FOV, 12 × 12 for the sagittal full-FOV, and 16 × 4 for the axial reduced FOV cases. As a result of this method, each single-shot  $k$ -space data is first phase corrected, followed by complex averaging over all the repetitions. After the refocusing reconstruction, the

FIG. 2. (a) Axial full-FOV image of a water/fat phantom. (b) The result of using 2D-selective RF pulse and  $180^\circ$  refocusing RF pulse pair to achieve a reduced FOV excitation. Note that in (b), the signal from fat on top is also suppressed. Both images were acquired using a 2DFT spin-echo sequence with  $12 \times 12 \text{ cm}^2$  FOV, with the only difference being the RF excitation pulse.



homodyne reconstruction (15) is applied on the resulting averaged partial  $k$ -space data to get the final DW image. The ADC maps in SI, AP and LR directions were calculated on a pixel-by-pixel basis, according to

$$\text{ADC}_{ii} = \frac{\ln |DW_0/DW_{ii}|}{b}, \quad [3]$$

where  $ii$  is one of SI, AP, or LR directions. Here,  $DW_0$  and  $DW_{ii}$  are the signal intensities of the pixels in the non-DW image (i.e.,  $b = 0$ ), and the diffusion-weighted image in direction  $ii$ , correspondingly. The isotropic diffusion-weighted image ( $DW_{iso}$ ) was obtained by taking the geometric average of all three DW images, and the corresponding ADC map ( $\text{ADC}_{iso}$ ) was calculated by taking the arithmetic average of all three ADC maps.

## RESULTS

### Phantom Experiment Results

Figure 2 shows the effect of using the 2D selective RF pulse and the  $180^\circ$  refocusing pulse pair to achieve a reduced FOV excitation. As seen in Fig. 2b, there is no outer volume excitation, and fat suppression is successfully achieved.

### In Vivo Imaging Results

Figure 3 shows the sagittal results for the full-FOV and the reduced FOV ss-EPI, with isotropic DW images and ADC maps shown for comparison. Note that three adjacent slices were acquired for reduced FOV ss-EPI imaging, and only the central slice is shown here for comparison. The reduced FOV ss-EPI provides two times higher resolution for the same readout time when compared to the full-FOV ss-EPI, with the trade-off being the lower SNR due to a four times smaller voxel size. Note that the smaller voxel size considerably reduces partial volume artifacts, most pronounced at CSF/spinal cord interfaces.

Figure 4 shows non-DW ( $b = 0$ ), isotropic DW ( $b = 500 \text{ s/mm}^2$ ) images, and corresponding ADC maps ( $\text{ADC}_{iso}$ ) for all three slices of the reduced FOV ss-EPI imaging. Note that the outer slices have less signal from the spinal cord, due

to the fact that the diameter of the spinal cord is around 1 cm. Therefore, for the outer slices, the 4-mm slice thickness may contain signal from both within and outside the spinal cord.

Shown in Fig. 5 are the results of high-resolution axial DWI of the cervical spinal cord with reduced FOV ss-EPI. These images demonstrate the feasibility of acquiring sub- $mm$  DWI of the spinal cord with this method.

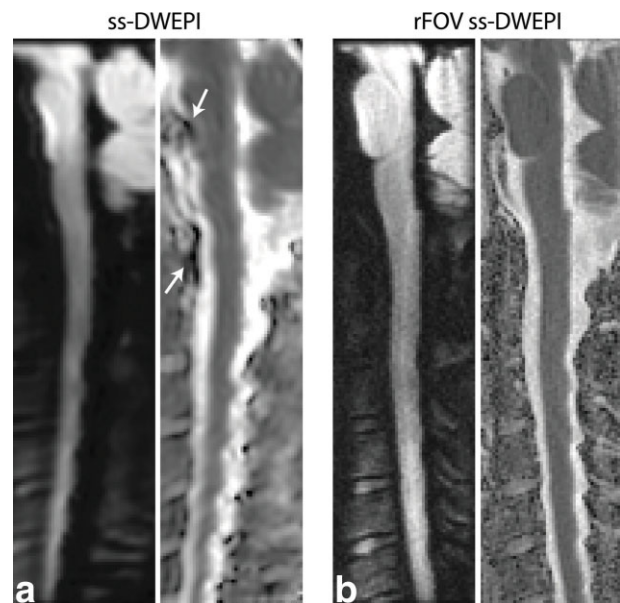


FIG. 3. Comparison results for (a) full-FOV ( $18 \times 18 \text{ cm}^2$ ) ss-DWEPI (only the  $18 \times 4.5 \text{ cm}^2$  region around the spine is displayed) and (b) higher resolution reduced FOV ( $18 \times 4.5 \text{ cm}^2$ ) ss-DWEPI. Shown are isotropic DW images ( $DW_{iso}$ ) and corresponding  $\text{ADC}_{iso}$  maps, from left to right. Both methods have the same readout time for comparison purposes. The resulting in-plane resolutions are (a)  $1.88 \times 1.88 \text{ mm}^2$  and (b)  $0.94 \times 0.94 \text{ mm}^2$ , with 4 mm through-plane slice thickness and  $b = 500 \text{ s/mm}^2$  for DW images. Note that the partial volume artifacts (the dark regions at the CSF boundary in ADC maps, as shown with the white arrows) are greatly reduced with reduced FOV ss-DWEPI due to higher resolution.

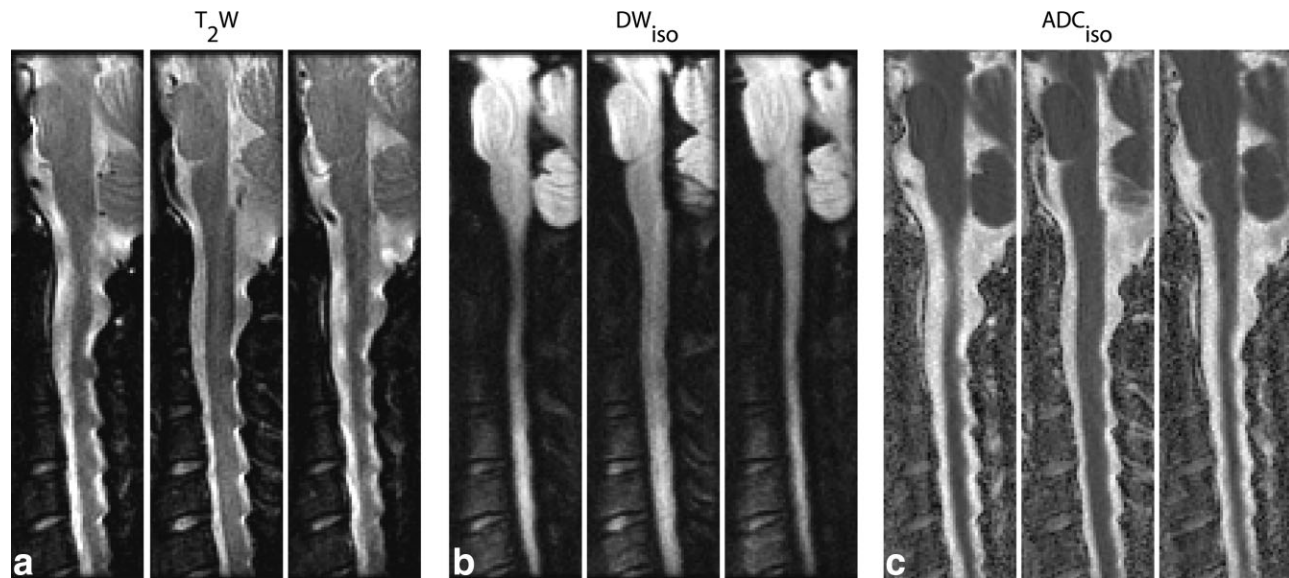


FIG. 4. Multi slice reduced FOV ss-DWEPI images of three adjacent slices. From left to right: (a)  $T_2$  weighted images ( $b = 0$ ), (b) isotropic DW images ( $DW_{iso}$ ), and (c) corresponding  $ADC_{iso}$  maps. ( $b = 500 \text{ s/mm}^2$ ,  $0.94 \times 0.94 \text{ mm}^2$  in-plane resolution, 4 mm slice thickness and 0.5 mm slice spacing). Note that only  $DW_{iso}$  images are shown here, even though DW images in SI, AP, and LR directions were first reconstructed separately to later form the  $DW_{iso}$  image.

## DISCUSSION

For DWI of the spinal cord, we have presented a reduced FOV ss-EPI method that actively excites the minimal FOV to image the region of interest. Reducing the FOV reduces the number of required  $k$ -space lines, enabling the acquisition of higher resolution images for a fixed scan time. Here, we have demonstrated that images with twice the resolution of regular ss-EPI can be obtained with the reduced FOV ss-DWEPI method. Diffusion weighting was applied in three orthogonal directions (with an additional  $b = 0$  image), resulting in about a 10-min scan time. Note that, this method can easily be extended to diffusion tensor imaging (DTI) of the spinal cord, by increasing the number of DW directions to six or more, which would result in a scan time of around 15–20 minutes, depending on the heart rate.

One of the main advantages of this method is its compatibility with contiguous multi slice imaging. Unlike the ZOOM-EPI method (6), a slice gap is not mandatory, since the neighboring slices are not excited by the 2D excitation pulse. However, as discussed previously, there is a limit on the maximum number of slices that can be imaged simultaneously. To increase the number of slices, more blips can be used with the drawback of a longer echo time. Outer volume suppression pulses as in (7) are not needed with this method, since the 2D excitation pulse actively excites only the parts of the volume that will be used for imaging. Furthermore, unlike using multiple 1D excitation pulses (8), here the resulting SNR does not depend on the number of slices. In contrast to parallel imaging methods (16), where the reduction in the required number of scan lines depends on the coil geometry, here the reduction depends only on the ratio of the desired FOV to the full FOV. Moreover, parallel imaging methods can be combined with

this method to further reduce the required number of scan lines.

## Fat Suppression

Note that in Fig. 4, fat suppression fails in certain regions, specifically in the bottom half of the images. This is due to a bending in the 2D echo-planar RF pulse profile that manifests itself only in non-axial images, because of the large FOV used in the physical z-direction of the scanner. The  $B_0$  field inhomogeneities become more pronounced with the large FOV, resulting in the bending of the excitation profile when combined with the long duration (16.8ms) and the concomitant magnetic field from the echo-planar gradients of the 2D RF pulse. In contrast, because the  $180^\circ$  refocusing RF pulse is relatively short, its profile remains unaltered. Consequently, the two profiles overlap only partially, resulting in the refocused slice having signal from both fat and water. Depending on the center frequency of the excitation, the slice may have no fat signal at the center and have increasingly higher percentage of fat toward the edges, or vice versa. Therefore, accurately setting the excitation frequency is important to achieve a proper fat suppression. Higher order shimming may further help overcome the problem by reducing some of the field inhomogeneities (17).

## Image Reconstruction

Because the image SNR is proportional to the voxel size, the reduced FOV images with twice the resolution have one-fourth SNR when compared with regular ss-EPI images in Fig. 3. When the individual (i.e., nonaveraged) DW images are SNR deficient as in this case, absolute value averaging of the images results in a rectified noise floor, which causes an

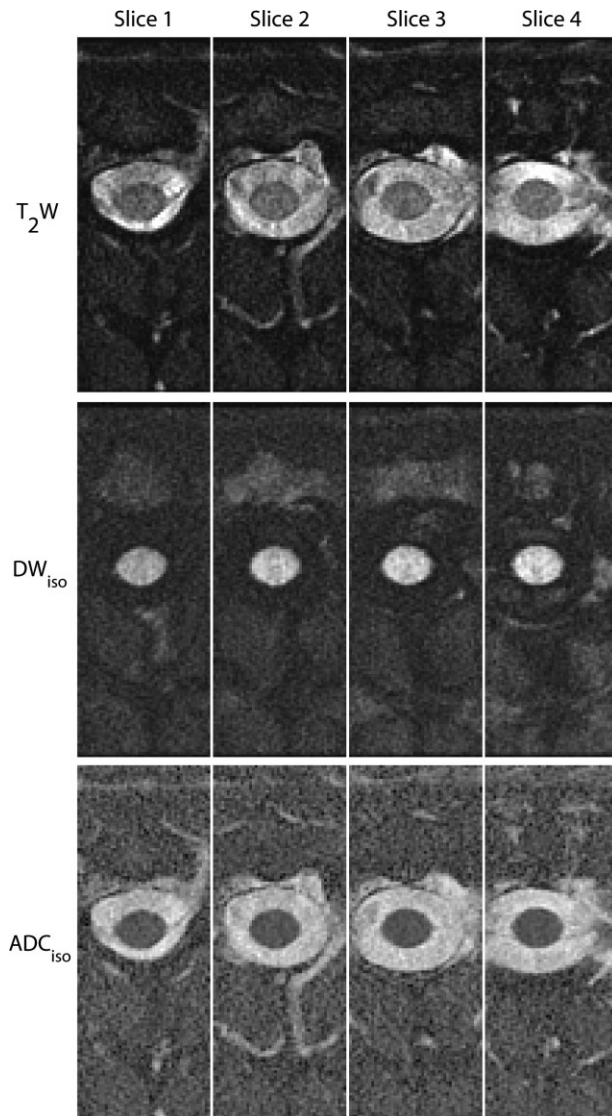


FIG. 5. Axial multi slice reduced FOV ss-DWEPI images of the cervical spinal cord. From top to bottom:  $T_2$ -weighted images, isotropic DW images ( $DW_{iso}$ ), and corresponding ADC maps ( $ADC_{iso}$ ) ( $b = 500$  s/mm<sup>2</sup>, FOV =  $8 \times 3$  cm<sup>2</sup>,  $0.62 \times 0.62$  mm<sup>2</sup> in-plane resolution, 5-mm slice thickness and 0.5-mm slice spacing).

underestimation of the ADC values in low SNR regions (18). Here, to avoid the effects of the rectified noise floor, ss-EPI images were complex averaged after correcting for shot-to-shot phase variations using refocusing reconstruction. The central 12.5% of  $k$ -space data from each single-shot DW image was used as the navigator data during refocusing reconstruction. The fact that there is no need for an additional navigator echo and that the center of  $k$ -space for each ss-EPI has exactly the same contrast as the original image makes this technique more robust compared to multi shot techniques [e.g. navigated IEPI (19–22)].

## ACKNOWLEDGMENTS

EUS thanks Brian A. Hargreaves, Tolga Cukur, and Daehoo Lee for all the discussions and help throughout the study.

## REFERENCES

- Bammer R, Fazekas F. Diffusion imaging of the human spinal cord and the vertebral column. *Top Magn Reson Imaging* 2003;14:461–476.
- Horsfield M, Jones D. Application of diffusion-weighted and diffusion tensor MRI to white matter diseases: A review. *NMR Biomed* 2002;15:570–577.
- Mikulis D, Wood M, Zerdoner O, Poncet B. Oscillatory motion of the normal cervical spinal cord. *Radiology* 1994;192:117–121.
- Anderson A, Gore J. Analysis and correction of motion artifacts in diffusion weighted imaging. *Magn Reson Med* 1994;32:379–387.
- Turner R, Bihan DL. Single shot diffusion imaging at 2.0 Tesla. *J Magn Reson* 1990;86:445–452.
- WheelerKingshott C, Hickman S, Parker G, Ciccirelli O, Symms M, Miller D, Barker G. Investigating cervical spinal cord structure using axial diffusion tensor imaging. *Neuroimage* 2002;16:93–102.
- Wilm B, Svensson J, Hennig A, Pruessmann K, Boesiger P, Kollias S. Reduced field-of-view MRI using outer volume suppression for spinal cord diffusion imaging. *Magn Reson Med* 2007;57:625–630.
- Jeong E, Kim S, Guo J, Kholmovski E, Parker D. High-resolution DTI with 2D interleaved multi slice reduced FOV single-shot diffusion-weighted EPI (2D ss-rFOV-DWEPI). *Magn Reson Med* 2005;54:1575–1579.
- Alley M, Pauly J, Sommer F, Pelc N. Angiographic imaging with 2D RF pulses. *Magn Reson Med* 1997;37:260–267.
- Stejskal E, Tanner J. Spin diffusion measurements: Spin echoes in the presence of a time-dependent field gradient. *J Chem Phys* 1965;42:288–292.
- Bito Y, Hirata S, Yamamoto E. Optimum gradient factors for apparent diffusion coefficient measurements. In *Proceedings of the 3rd Annual Meeting of Society of Magnetic Resonance, Nice*; 1995, p 913.
- Clark C, Baker G, Tofts P. Magnetic resonance diffusion imaging of the human cervical spinal cord in vivo. *Magn Reson Med* 1999;41:1269–1273.
- Bruder H, Fischer H, Reinfelder HE, Schmitt F. Image reconstruction for echo planar imaging with nonequidistant  $k$ -space sampling. *Magn Reson Med* 1992;23:311–323.
- Miller K, Pauly J. Nonlinear phase correction for navigated diffusion imaging. *Magn Reson Med* 2003;50:343–353.
- Noll D, Nishimura D, Macovski A. Homodyne detection in magnetic resonance imaging. *IEEE Trans Med Imaging* 1991;10:154–163.
- Cercignani M, Horsfield M, Agosta F, Filippi M. Sensitivity-encoded diffusion tensor MR imaging of the cervical cord. *AJNR Am J Neuroradiol* 2003;24:1254–1256.
- Spielman D, Adalsteinsson E, Lim K. Quantitative assessment of improved homogeneity using higher-order shims for spectroscopic imaging of the brain. *Magn Reson Med* 1998;40:376–382.
- Jones D, Basser P. Squashing peanuts and smashing pumpkins: How noise distorts diffusion-weighted MR data. *Magn Reson Med* 2004;52:979–993.
- Ordidge R, Helpert J, Qing Z, Knight R, Nagesh V. Correction of motional artifacts in diffusion-weighted MR images using navigator echoes. *Magn Reson Imaging* 1994;12:455–460.
- de Crespigny A, Marks M, Enzmann D, Moseley M. Navigated diffusion imaging of normal and ischemic human brain. *Magn Reson Med* 1995;33:720–728.
- Butts K, de Crespigny A, Pauly J, Moseley M. Diffusion-weighted interleaved echo-planar imaging with a pair of orthogonal navigator echoes. *Magn Reson Med* 1996;35:763–770.
- Atkinson D, Porter D, Hill D, Calamante F, Connelly A. Sampling and reconstruction effects due to motion in diffusion-weighted interleaved echo planar imaging. *Magn Reson Med* 2000;44:101–109.